

Temporal change in *P*-wave scatterer distribution associated with the *M*6.1 earthquake near Iwate volcano, northeastern Japan

S. Matsumoto,^{1,*} K. Obara,² K. Yoshimoto,³ T. Saito,³ A. Ito⁴ and A. Hasegawa³

¹Faculty of Engineering and Resource Science, Akita University, Akita, 010-8502, Japan

²National Research Institute for Earth Science and Disaster Prevention, Tsukuba 305-0006, Japan

³Graduate School of Science, Tohoku University, Sendai 980-8578, Japan

⁴Faculty of Education, Utsunomiya University, Utsunomiya 320-0003, Japan

Accepted 2000 September 20. Received 2000 September 18; in original form 2000 March 20

SUMMARY

Temporal variation of the scatterer distribution has been detected around the focal area of an *M*6.1 earthquake, northeastern Japan, by applying semblance analysis to seismic array data. The variation was found in slant-stacked waveforms of two explosions detonated just above the focal area one month before and two months after the *M*6.1 earthquake. According to geodetic observations, a pressure source that might be a magma reservoir exists beneath this region and its location changed during the observation period. Slant-stacked waveforms are slightly different for the two explosions. The difference suggests that a scatterer contributing to the coda part is shifted towards the east and to greater depths only after three months. In this region, seismic and volcanic activity was very active during the interval between the two explosions. The volcanic activity of Mt Iwate just north of the *M*6.1 earthquake, which started several months beforehand, continued during this period. It may be considered that scatterer change relates to seismic and/or volcanic activity in the studied area.

Key words: array, crustal structure, inhomogeneous media, scattering, seismic coda, temporal change.

1 INTRODUCTION

Recent observations with high-resolution techniques have allowed us to detect and study a temporal change of the crustal structure associated with seismic and volcanic activity. There have been numerous efforts to monitor temporal variations of crustal inhomogeneity. Poupinet *et al.* (1984) detected velocity variations associated with the Coyote Lake, California, earthquake (*M*5.9) using an earthquake doublet. As described in a review paper by Sato (1988), changes in the coda duration and attenuation reflect temporal variation of crustal heterogeneity. In a detailed study, Got & Fréchet (1993) discussed the origin of temporal amplitude variations using seismic doublets and they detected the change in coda *Q* value. Karageorgi *et al.* (1997) found that a wavelet propagating in a localized region shows temporal change related to the structure of the fault zone.

The northwestern part of Iwate Prefecture (NW Iwate) in the northeastern part of Japan is located in the Ou Backbone Range. The range, bounded at its eastern and western edges

by active faults, is a mountain chain running through the middle of the northeastern Japan arc parallel to the Japan trench, which is formed by a horizontal compressive stress field oriented almost in an east–west direction. The volcanic front passes through the range in a north–south direction (that is, almost parallel to the trench and the range). A large tectonic earthquake (*M*7.2) with a reverse fault type occurred at the western edge of this range in 1896. Mt Iwate volcano, which is located in this area, is one of the active volcanoes in northeastern Japan. A low-velocity region and active low-frequency earthquakes have been found beneath the volcano (Hasegawa & Yamamoto 1994). Since January 1998, both high seismic activity and notable crustal deformation have appeared at Mt Iwate (Ueki *et al.* 1999; Sato & Hamaguchi 1999; Tanaka *et al.* 1999; Miura *et al.* 2000). The observed crustal deformation data suggest that a pressure source exists beneath Iwate volcano. The source may be related to a magma reservoir that perhaps exists beneath Iwate volcano. Therefore, volcanic activity is considered to be higher in the region.

In this region, an *M*6.1 earthquake occurred on 1998 September 3 (Umino *et al.* 1998). The earthquake was located about 10 km southwest of Mt Iwate. A temporary seismic observation network has been deployed in the range to study

* Now at: Institute of Seismology and Volcanology, Faculty of Sciences, Kyushu University, Shimabara 855-0843, Japan.
E-mail: matumoto@sevo.kyushu-u.ac.jp

crustal inhomogeneity since 1997 (Hasegawa & Hirata 1999). An explosion experiment was carried out in this area by the Research Group for Explosion Seismology (RGES) in August 1998 (Hirata *et al.* 1998; RGES 1999). One of the shots, called M10, is located just above the fault area of the M6.1 earthquake. The second explosion, called M10R, was detonated at the same location as M10 after the occurrence of the earthquake. By analysing waveform data from the two explosions, Nishimura *et al.* (2000) and Nakamura *et al.* (2000) recently detected a 0.3–1 per cent velocity change in the focal area of the earthquake.

Seismic array observations can detect small-scale structure changes because the directional sensitivity of the array can be tuned to a target direction. Generally, many phases appear after direct *P*- and *S*-wave arrivals in seismograms of natural earthquakes and artificial explosions. These phases can be interpreted as waves scattered by inhomogeneities distributed within the crust. Nishigami (1991, 2000) and Revenaugh (1995) estimated scatterer distributions in the crust from large-amplitude phases in the coda part observed by seismic networks with station separations of several kilometres. Matsumoto *et al.* (1999) analysed seismograms recorded by a small-aperture seismic array and determined scatterer distribution in the crust beneath the Ou Backbone Range. They concluded that the scatterer distribution is spatially related to seismic activity. In the present study, we analyse seismic array data from the two explosions (M10 and M10R) in order to detect the temporal variation of crustal inhomogeneity and discuss its relation to seismic and volcanic activity.

2 OBSERVATION AND DATA

In order to detect scattered waves generated by inhomogeneities in the target area, we carried out a seismic array observation from 1998 August 1 to November 12 in the Ou Backbone Range of northeastern Japan. The array was composed of 2 Hz vertical-component seismometers and 1 Hz three-component seismometers with a site spacing of 10–40 m. Vertical- and three-component seismometers were installed at 96 and 32 sites, respectively. The length of the array is about 3 km. The location and configuration of the array are shown in Fig. 1. Seismometers were distributed two-dimensionally in order to detect scattered waves coming from various directions. Seismic signals were collected through CDP cable, commonly used in exploration seismology, and recorded by a digital recorder system. The system, with 192 channels, was equipped with a sigma-delta A/D converter with 24-bit resolution. The recording time for each event was set at 60 s with a sampling frequency of 500 Hz. Waveform data from explosions, carried out by RGES (1999), were recorded by manual triggering.

In the present study, we analyse waveform data from 2 explosions (M10 and M10R) whose locations are shown in Fig. 1. Shot M10R is 29 m north and 2.8 m east of the first shot, M10. 150 kg of dynamite was detonated in boreholes on August 10 (one month before the M6.1 earthquake) and November 2 (two months after the earthquake occurred). Record sections for shots M10 and M10R are shown in Fig. 2. Waveform data were filtered between 6 and 10 Hz with a decay of -12 db Oct $^{-1}$. The coda part was then amplified by AGC (auto gain control) processing with a window length of 4 s. In Fig. 2, several phases are clearly visible. These phases can be identified in the record section even without AGC amplitude

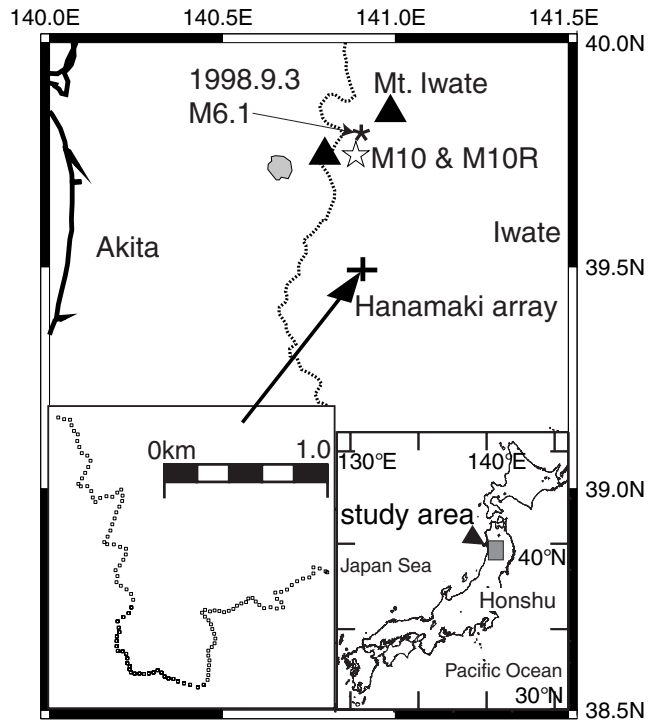


Figure 1. Map showing locations of seismic array and two explosions. Stars show shotpoints of explosions M10 and M10R in 1998. Cross denotes location of Hanamaki array. Asterisk shows epicentre of 1998 M6.1 earthquake. Solid triangles denote locations of active volcanoes. Array profile is shown in the lower left, open squares being observation sites.

recovery processing. In the following section, array analysis is applied to these data in order to estimate the spatial distribution of reflectors or scatterers in detail.

3 BEAM FORMING

For scattered wave beam formation coming into the array, we apply slant-stack processing to the observed array data from the explosions. The slant stacking is also called ‘delay sum beam forming’. A slant-stacked waveform in a certain azimuth and slowness can be considered as scattered waves coming from that direction along the ray path with that slowness. In this study, we discuss the difference in slant-stack waveforms for M10 and M10R. If we detect a difference between the slant-stacked waveforms based on the two shots, we can locate the origin of the waveform’s temporal change from the stacking direction, the lapse time and the hypocentre location. The slant-stacked waveforms for M10 and M10R were composed of 108 vertical seismometer signals with high signal-to-noise ratios (snr) for both shots. Comparing stacked waveforms of M10 with waveforms of M10R by slowness and azimuth, we try to find any temporal change of inhomogeneity in the crust.

The local subsurface structure is different from site to site since the length of the array profile is more than 3 km. Therefore, the time axis at each site is shifted by the static correction time to remove the effect of shallow subsurface structures before slant stacking. For shot M10, we obtain a time difference at each site by subtracting the manually picked time from the calculated time of the direct *P*-wave arrival that is determined from an optimum direct *P*-wave front of the

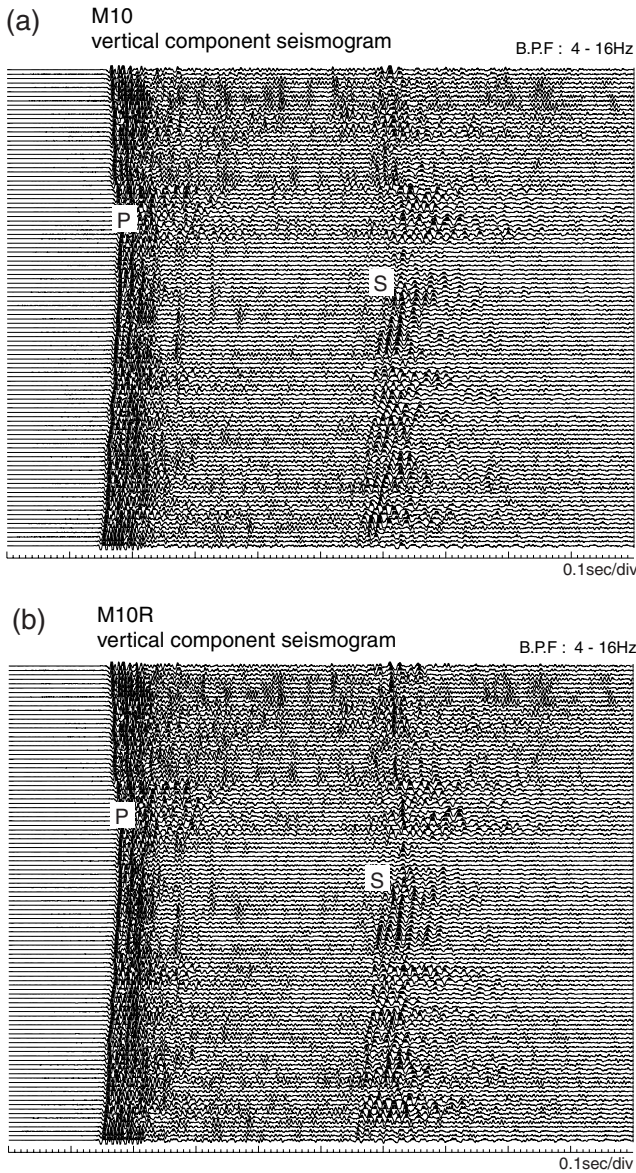


Figure 2. Record sections of vertical-component seismometers used in our analysis. (a) and (b) are the sections for M10 and M10R, respectively. Waveforms were bandpass filtered from 4–16 Hz with -12 db oct $^{-1}$ decay.

corresponding shot. The optimum wave front is determined by fitting the plane wave to the picked arrival time of a direct P wave. Next, we obtain the static correction time at each site, which ranges from -0.017 to 0.029 s. In order to evaluate the effect of static correction, we check the semblance coefficients for a direct P wave before and after applying the static correction. The semblance coefficient is defined as

$$s(t) = \frac{\sum_j^M \left[\sum_i^N A_i(t + \Delta t_{ij}) \right]^2}{N \sum_j^M \sum_i^N A_i^2(t + \Delta t_{ij})}, \quad (1)$$

where $A_i(t)$ is the waveform observed at the i th station, N is the number of stations and M is the number of samples in a given time window. Δt_i is calculated from the assumed ray direction

and the location of the i th station. By applying static correction, we were able to determine that the maximum semblance value of a direct P wave increased to 0.5 from 0.3 after the grid search described later.

We assume here that scattered waves approach an array as plane waves. The curvature of the wave front of scattered waves affects the amplitude of slant-stacked waveforms and semblance coefficients. For instance, if the time difference between an actual spherical wave front and an assumed plane wave front at the edge of the array were greater than half of the period of a bandpass filtered seismogram, the signals of the scattered waves would not be emphasized, while the number of stacked waveforms would increase because of their inverse polarity. Taking into account the frequency of seismic waves, the P -wave velocity (i.e. higher than 5 km s^{-1} , see later) and the aperture of the array in this study, such an effect will not occur in the case where waves are generated by a scatterer at least 1 km away from the array.

The ray direction of a direct P wave is estimated by grid searching the maximum semblance value in a range. The range is from -0.2 to 0.2 s km^{-1} in slowness and from 0 to 180° in azimuth. Here ‘positive slowness’ means waves travel in the direction defined by the azimuth from the array. For instance, when an azimuth is $N0^\circ$, waves with positive and negative slownesses propagate from south and north to the array, respectively. Search intervals are at 0.1° and 0.005 s km^{-1} for the azimuth and slowness, respectively. A time window to calculate the semblance value is set at 0.2 s (i.e. $M=100$ samples in eq. 1). The direction of M10 is an azimuth of $N8^\circ\text{E}$ and a slowness of -0.17 s km^{-1} , which coincides with that for M10R with a discrepancy of less than 0.1° and 0.005 s km^{-1} in azimuth and slowness, respectively. The coincidence of the estimated direct P -wave directions between M10 and M10R suggests that there is no change in source location or observation system between the two explosions within the resolution of the grid search interval mentioned above.

On the other hand, the geographical azimuth to the epicentre of M10 is $N3^\circ\text{E}$. This value is different from that estimated from the direct P -wave arrivals by using the semblance analysis. This mismatch of the direct P -wave direction is perhaps caused by the local velocity anomaly along the ray path. Using the present data set, we cannot determine the actual effect on this mismatch. Therefore, we can only discuss the relative direction of scattered waves as it relates to that of the direct P wave.

4 DETECTING WAVEFORM CHANGE

In order to detect the change in waveform from M10 to M10R, we analysed the temporal variation of three parameters, that is, the cross-power spectrum, the phase delay and the coherence between the waveforms of the two explosions. The spectrum parameters at a certain lapse time are calculated in a fixed time window, which is cosine tapered (10 per cent of the edge data). After fast Fourier transforming the data, we estimate these parameters for a fixed frequency range in each case. We adopt two frequency ranges of 4–8 and 8–16 Hz to estimate cross-power, phase delay and coherence. Cross-power and coherence are averaged in the frequency range. Phase delay can be estimated from the gradient of the phase spectrum in the frequency domain. Therefore, the delay is obtained by first regression fitting to the phase spectrum. The time window lengths are 0.6 and 0.3 s for the 4–8 and 8–16 Hz ranges, respectively.

Initially, we checked variations of waveforms observed at several stations of the array. Fig. 3 shows the time sequence of the three parameters for the 4–8 Hz range with a 0.1 s time window. Vertical bars show estimation errors of the phase delay time based on the trend of the phase spectrum in the given frequency range. Filtered seismograms corresponding to the frequency range are also plotted as references for both M10 (solid line) and M10R (dashed line). In these sequences, no phase delay is noted between the two explosions until direct S-wave arrival times. This result suggests two possibilities. One is that no temporal variation of the crustal structure occurred for 3 months. The second is that the variation cannot be detected by these single-station records alone. In the second case, scattered waves resulting from temporally varying inhomogeneities are masked by scattered waves coming from other places without variation and/or by background local noise

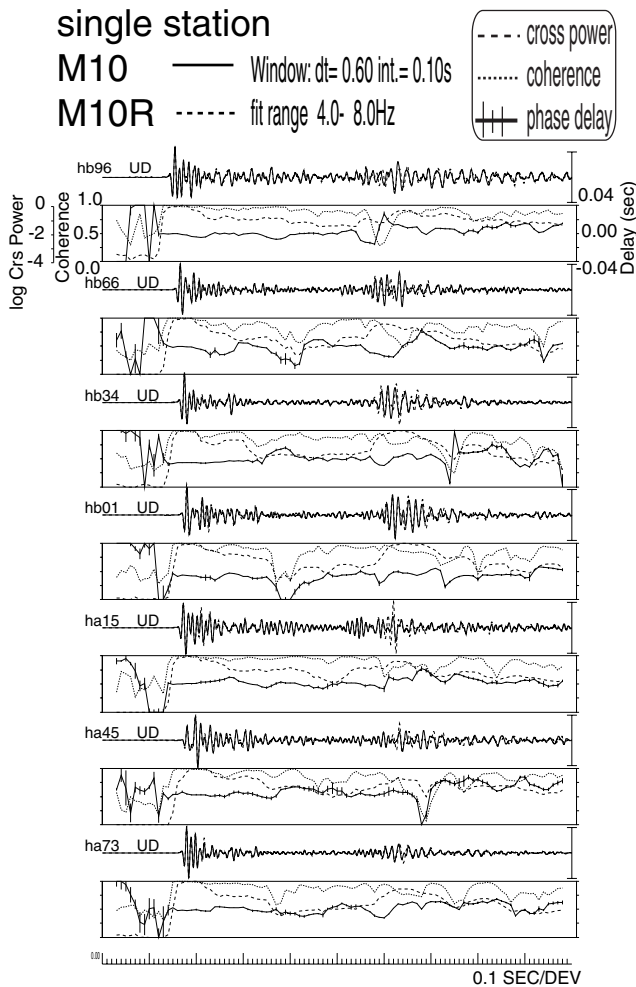


Figure 3. Temporal variations of cross-power spectra, phase delay and coherence between waveforms for two explosions observed at several stations. Dashed, dotted and solid lines are cross-power spectra, coherence and phase delay for the 4–8 Hz range, respectively. Phase delay was obtained by regression fitting to the phase spectrum in the frequency range. The time window length was 0.6 s for 4–8 Hz. The moving interval of the time window was 0.1 s. Vertical bar indicates estimation error of phase delay time obtained from the trend of the phase spectrum in the given frequency range. Filtered seismograms of the corresponding frequency range are also plotted for both M10 (solid line) and M10R (dashed line) for reference.

around the array. The background noise is independent of the source time function of an explosion (e.g. artificial noise or a microseism). In fact, the ratio of the seismic signal to background noise (the snr) is high enough to exclude a contribution of background noise to the seismogram during the several seconds after direct P-wave arrival (T_p). Therefore, the observed waveform apparently did not change within the given time lapse, even though the crustal structure did change during the three months between the two explosions.

As the next step, we apply the same analysis to slant-stacked waveforms. Figs 4 and 5 show time sequences of the three parameters in the 4–8 and 8–16 Hz ranges for variable slowness values with a fixed azimuth in the direct P-wave direction ($N8^\circ E$). The moving interval of the time window is 0.1 s. In the 4–8 Hz range, the phase delay drastically changes from 2 to 3 s after T_p . The delay in this part is about 30 ms, in contrast to the delay times seen in the earlier lapse time. After a lapse time of 3 s from T_p , the delay becomes smaller than 5 ms again until the direct S-wave arrival (T_s). After T_s , the delay becomes unstable. This notable delay change is not so clear for the higher frequency range of 8–16 Hz (Fig. 5). The phase delay sequence maintains a steady state, smaller than 5 ms, prior to T_s .

For the direct P wave, the phase difference is small and the coherence is high for both frequency bands based on the present analysis. This suggests that, for P-wave radiation, the source

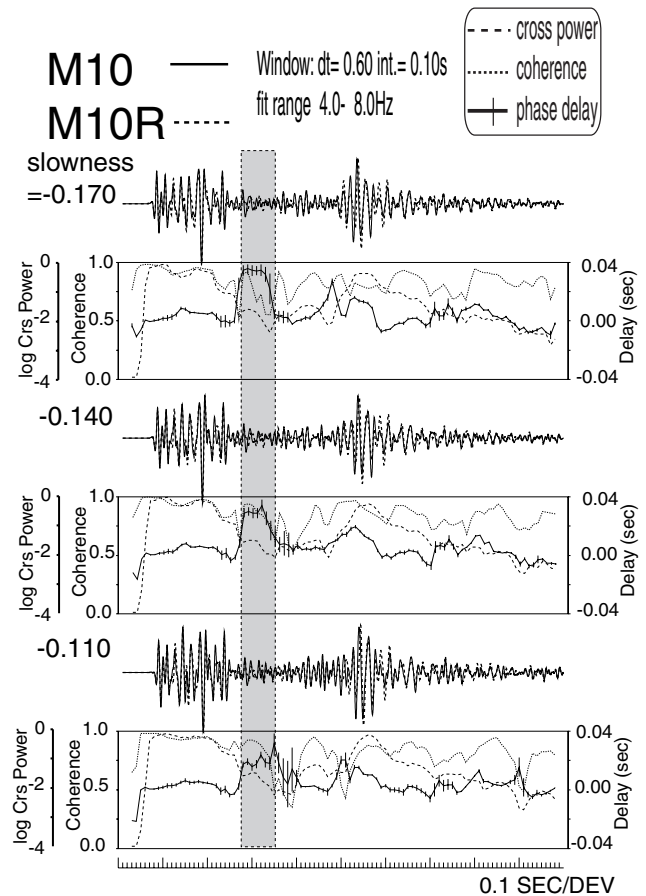


Figure 4. Temporal variations of the same parameters as in Fig. 3 but for slant-stacked waveforms in the 4–8 Hz range. Slant-stacked waveforms with slownesses of -0.17 , -0.14 and -0.11 in azimuth of the explosion hypocentre are used. Shaded region shows a drastically changed part in the phase delay sequence.

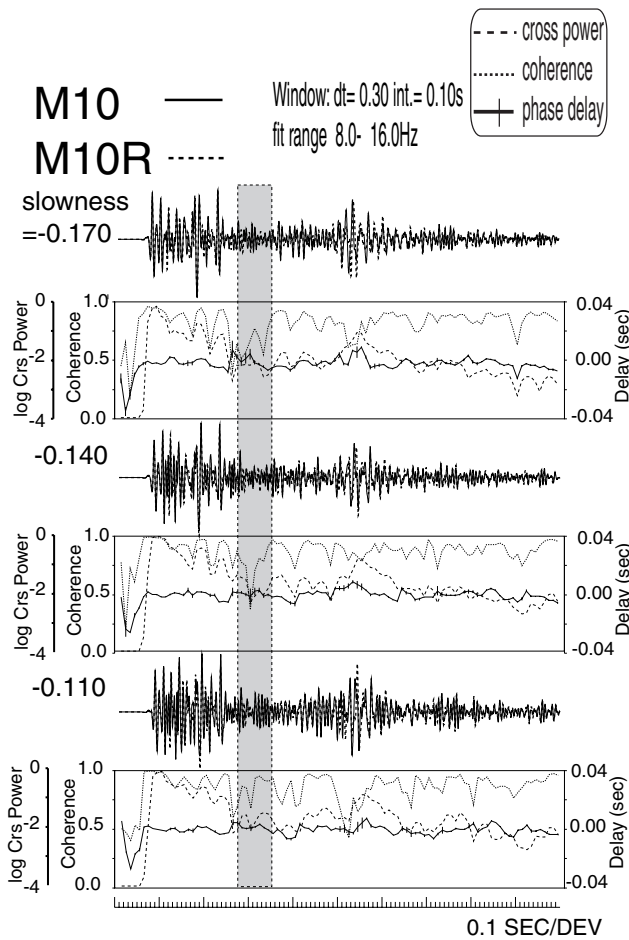


Figure 5. Same as Fig. 4 except for a frequency range of 8–16 Hz and a window length of 0.3 s with a 0.1 s moving interval.

time function of M10 coincides with that of M10R. On the other hand, the phase delay of a direct *S* wave from M10 to M10R is about 20 ms, which suggests that their source time functions are different from each other. The phase delay of 30 ms observed 2 s after T_p cannot be explained by a difference in the *S* wave source time function because the delay should amount to 20 ms when the phase is composed of an *S*–*P* converted wave. Moreover, the *S*-wave energy radiated from the explosion source is much smaller than the *P*-wave energy. Based on the above discussion, it is reasonable to assume that the temporally changed phase is composed of *P*–*P* scattered waves resulting from crustal inhomogeneity, although we cannot completely exclude the possibility that the phase is composed of *S*–*P* scattered waves. Of course, it is possible that the 30 ms phase delay is caused by both a change in the *S*-wave source time function and a change in the *S*–*P* scatterer location.

For the seismogram after T_s , it is very likely that the change in the source time function for the *S* wave contributes to a variation in the waveform as a result of *S*–*S* scattering. Therefore, we discuss only the large phase delay at 2 s after T_p observed in the 4–8 Hz range in the present study.

5 ORIGIN OF VARIATION

We calculated the semblance distribution in the slowness domain in order to determine in detail the ray direction of the wave

arriving at the array. The distribution is obtained by calculating the semblance value for the 2-D slowness (s_x for N–S, s_y for E–W) from -0.2 to 0.2 s km $^{-1}$ with a 0.0025 s km $^{-1}$ interval. The time window is set to 0.2 s. In this calculation, we apply the static corrections previously mentioned. The results for the direct *P* wave and for the 0.2 s periods before, at and after the phase delay anomaly are shown in Figs 6 and 7 for the 4–8 and 8–16 Hz ranges, respectively.

Fig. 6 shows that the pattern for the direct *P* wave of M10 is the same as that of M10R. This means that the source locations are the same under the resolution by the present analysis. This pattern also illustrates the response of the array deployed in the present study. There are no differences in the pattern, apart from the anomalous part between the two explosions, as can be seen in Figs 6(b) and (d). This means that the source, the instruments and the crustal structure corresponding to the present lapse time window have not temporally changed during the three months between the explosions. However, the peak slowness vector for M10 is slightly different from that for M10R during the phase delay anomaly period (Fig. 6c). Not only did the semblance pattern change, but also the peak semblance value decreased from 0.13 for M10 to 0.056 for M10R. In the 8–16 Hz range, the semblance distribution for M10 has a similar pattern to that for M10R, even in the phase delay anomaly period (Fig. 7c). These results show that the temporal variation of the crustal structure can be seen for propagating waves with longer wavelengths. A decreased maximum semblance value implies that the energy of scattered waves becomes relatively weak. Therefore, it appears that the scattering strength also changed, becoming smaller during the three months. The scatterer distribution might not have changed for three months for the higher-frequency band of 8–16 Hz; however, the semblance value in the 8–16 Hz range is not always highest for the degree of slowness showing the maximum value in the 4–8 Hz range. This means that scattered energy coming from a given direction is masked by scattered waves from other directions because of the weak contribution of energy to the coda part, due to the small scattering coefficients for the higher frequency range.

We can estimate the temporally changed scatterer location by calculating the ray path of scattered waves, from the slowness vector, the traveltime of the wave and the velocity structure. We assume here that *P*-wave velocity is given as

$$V(z) = 5.3 + 0.058z \text{ km s}^{-1},$$

where V is the *P*-wave velocity and z is the depth in kilometres. This structure model agrees with that for hypocentre determination in this area (Umino *et al.* 1998) and explains the traveltime data of the direct *P* wave for M10 and other explosions detonated in this area. Fig. 8 shows scatterer locations estimated in this manner. Shaded areas imply semblance values higher than 80 per cent of the maximum value of each semblance distribution. White lines represent contours of 90 per cent of the maximum value. Open circles show hypocentres from 1998 September 3 to November 2 determined by Tohoku University by using temporary seismic network data. The detected scatterer changed its location towards the east and at depth in the crust. Before the *M*6.1 earthquake occurrence, the scatterer was located around the hypocentre. The scatterer changed its location below the aftershock area after the *M*6.1 event. This location change occurred within only

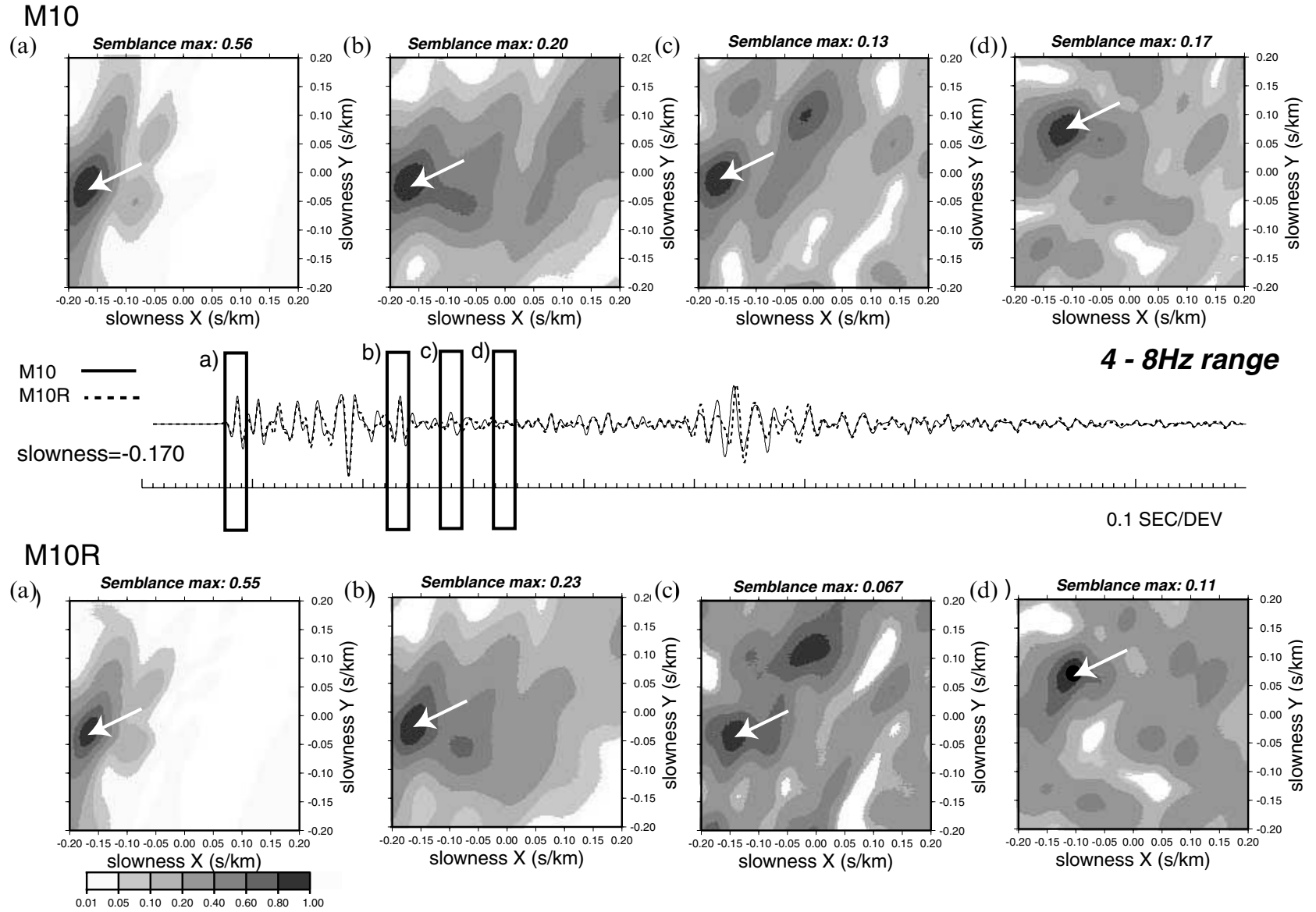


Figure 6. Semblance distribution versus various slownesses for 4–8 Hz. The greyscale denotes semblance values normalized by the maximum semblance value (indicated by white arrows). The distribution was calculated by using records at 108 sites. Upper and lower figures show the results for shots M10 and M10R, respectively. As an example of a slant-stack waveform, the waveform with the slowness in the direct *P*-wave direction is shown in the middle. Solid and dashed lines are waveforms for M10 and M10R, respectively. (a)–(d) in the upper and lower figures are the results obtained by analysing waveforms in the time windows shown in the middle.

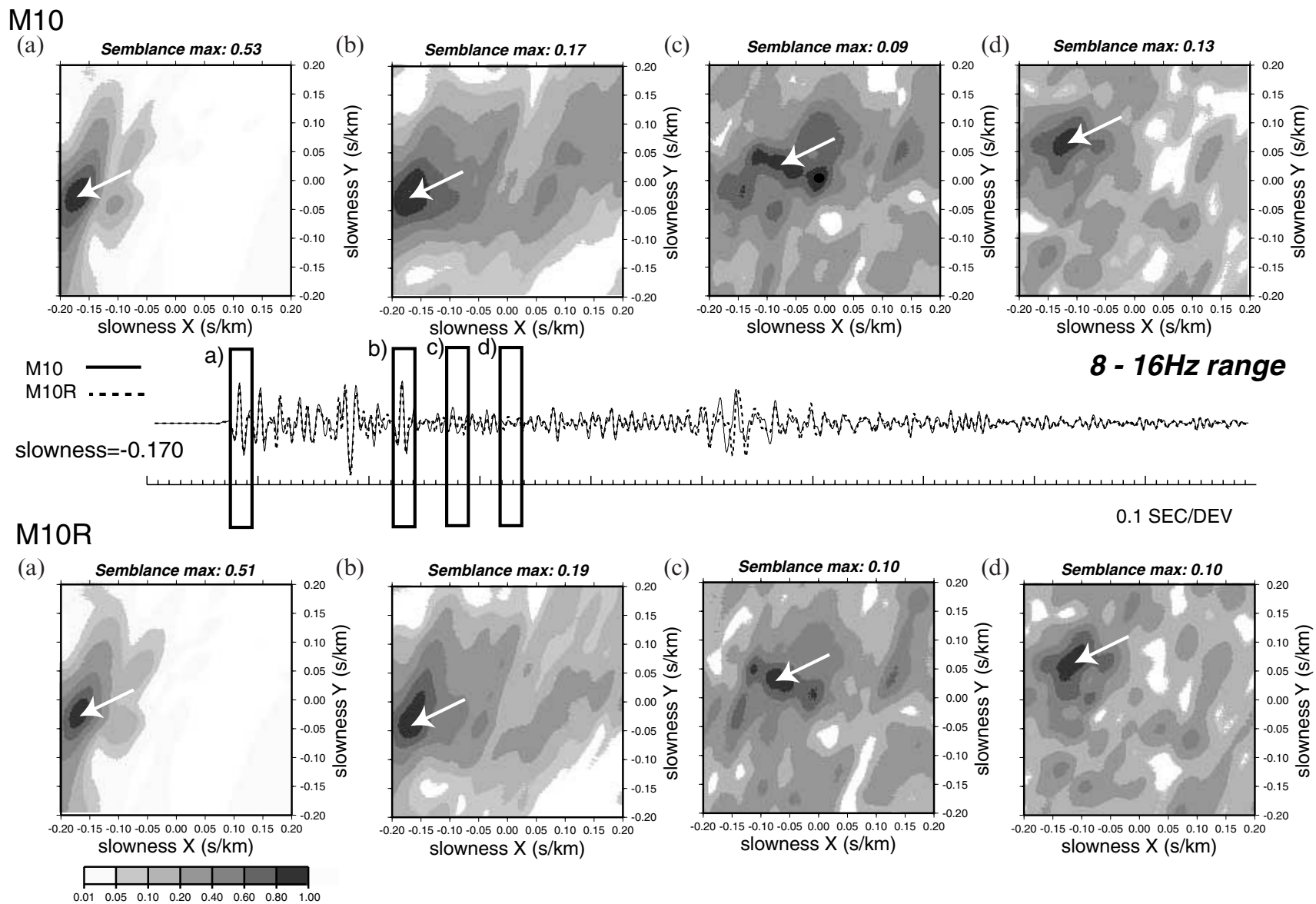


Figure 7. Same as Fig. 6 but for 8–16 Hz.

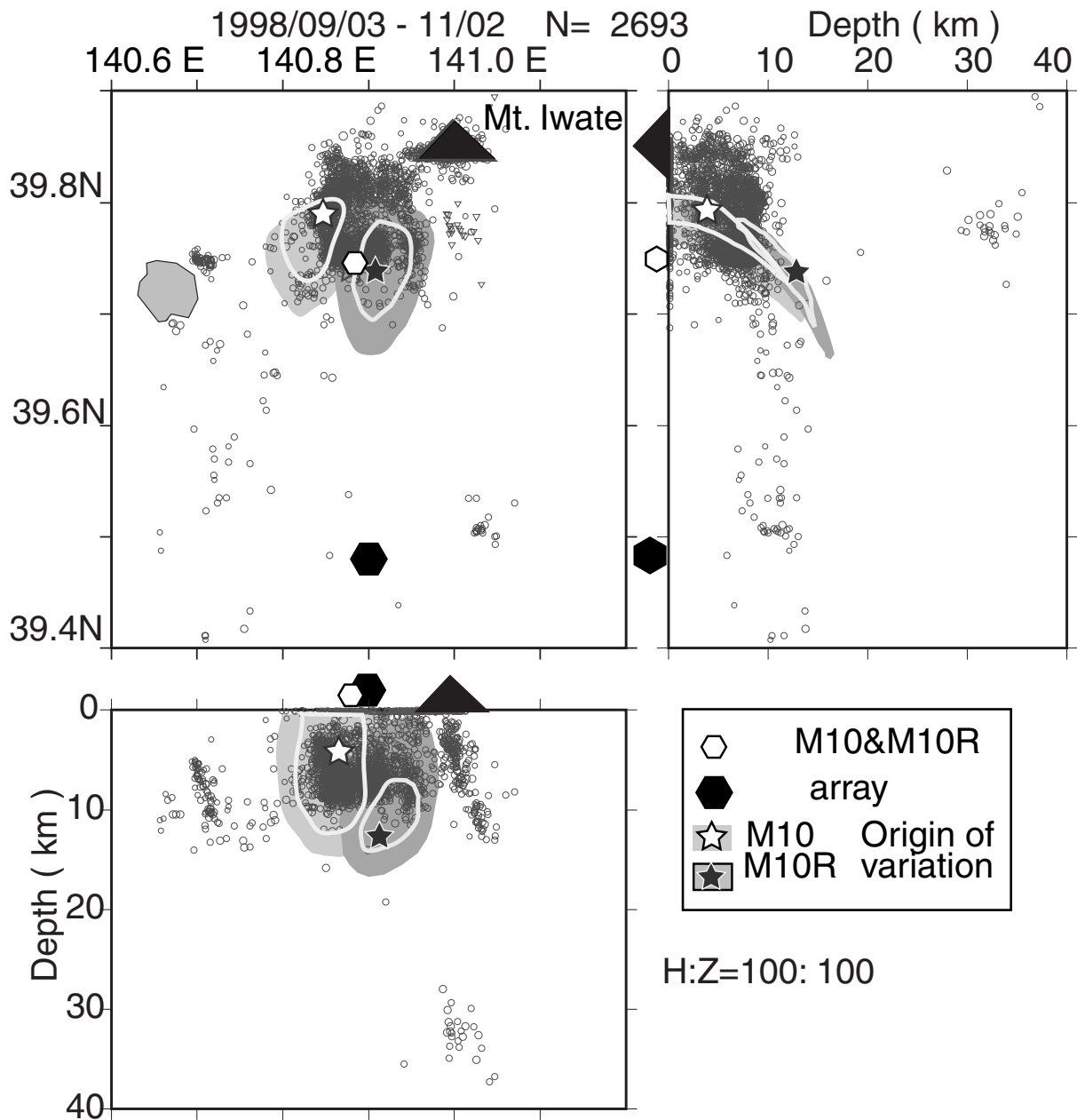


Figure 8. Shift of the scatterer location. Open star shows location of the scatterer obtained from M10. Solid star shows that from M10R. Shaded areas are those with semblance values higher than 80 per cent of the maximum value. White lines denote the 90 per cent contour of the maximum value. Small open circles are hypocentres from 1998 September 3–November 2 determined by Tohoku University using temporary seismic network data.

three months. Inhomogeneity for an elastic medium would not change in such a short time; it requires a geological timescale. Therefore, the present result suggests that fluid movement caused the inhomogeneity variation found.

Higher semblance values equal to 80 per cent or more of the maximum value for both explosions in Fig. 8 cover an area about 10 km wide. This is reflected by the response of the array deployed in the present observation. In order to ascertain the effect of the array response and the resolution of our analysis, we carried out a reconstruction test for the scatterer locations obtained. The synthetic waveform for each station of the array is composed of a sine wave with a 6 Hz cycle length that is delayed with the time calculated from the slowness of the waves

from the scatterer temporally changed. To obtain semblance distributions for both explosions, we applied semblance analysis to the synthetic scattered wave for various degrees of slowness (Fig. 9). The distribution of the semblance values thus obtained reflects the array response. A comparison of simulated and observed results shows similar patterns around the maximum semblance value. In other words, the observed pattern of semblance distribution is well reconstructed by the simulation. This means that the spread of the high semblance area does not reflect the actual extent of the scatterer's existing area but is caused by the array response. The agreement of the simulated and observed results shows that the difference in scatterer locations between M10 and M10R is significant.

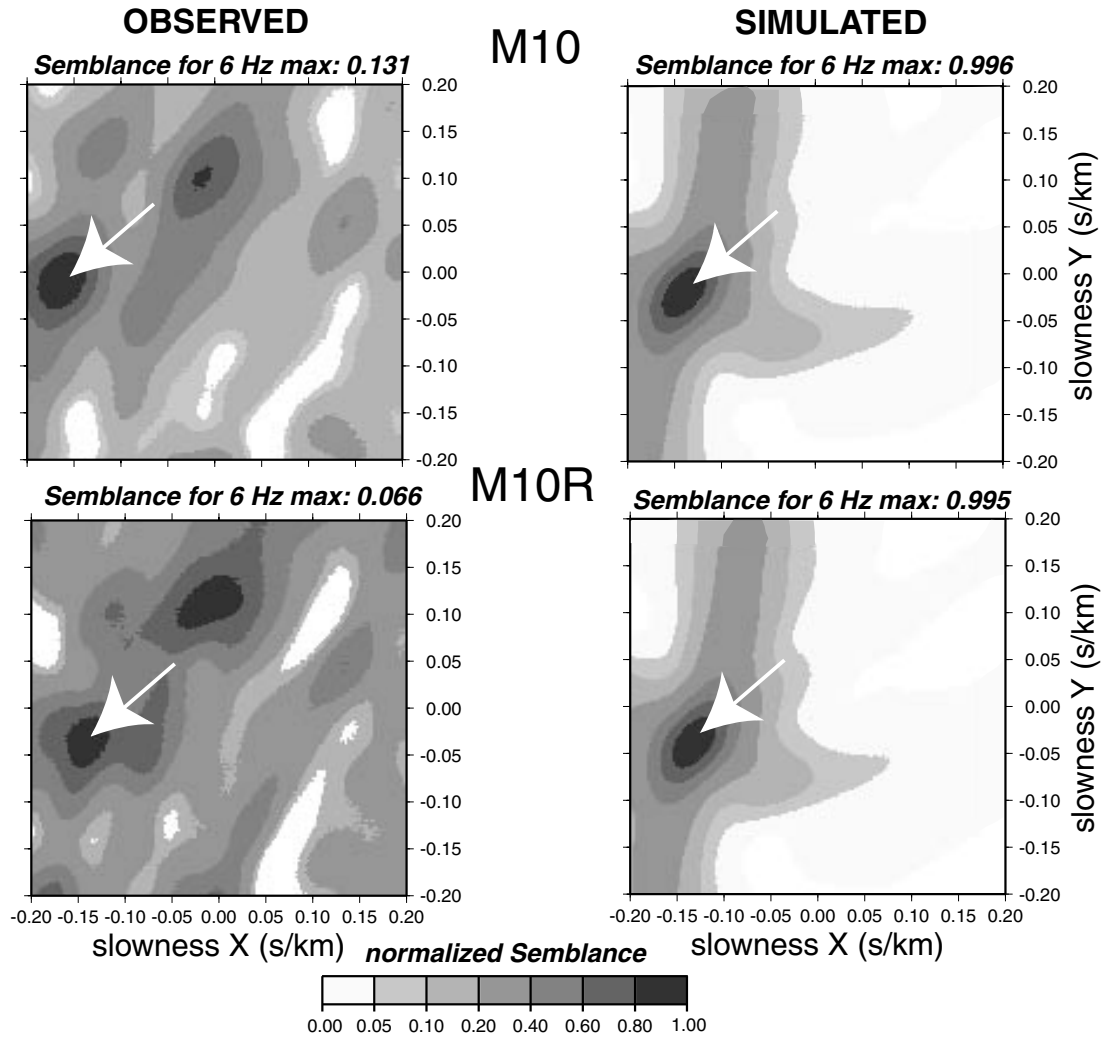


Figure 9. Comparison of simulated semblance distribution in 4–8 Hz range with the observed distribution for various slowness values. The distribution is calculated by using records at 108 sites. White arrows show the slowness with the maximum semblance value.

The semblance value obtained here is small—0.067—for M10R. The semblance value does not increase in the same way as the value of the direct *P* wave for the following reasons. First, if N traces composed of random noise are stacked in order to obtain a semblance value, that semblance value should become $1/N$ according to eq. (1). In this study, the semblance values are obtained from records from 108 channels; the value for random noise thus becomes 0.0093. This value is much smaller than that for M10R seen in Fig. 6(c). Therefore, the semblance values discussed in our analysis are not caused by an effect of random noise. Next, we list in Table 1 the root mean square amplitudes and their standard deviations for 108 traces in the parts of noise, direct *P* waves and *P* coda shown in Fig. 6(c), because the amplitude of a seismic trace directly affects the estimation of semblance, as expected from eq. (1). The amplitudes in the noise part are less than 10 per cent of those in the direct *P*-wave and *P*-coda parts, which is equivalent to having no ground noise effect, such as that caused by artificial noise and/or microseisms, on the semblance estimation in this study. The maximum value of the semblance coefficient is theoretically expected to be 1.0. This value is realized in the

Table 1. Root mean squared amplitude in the 4–8 Hz range (avr.), its standard deviation (std.) for the array, and expected and observed semblance values for shots M10 and M10R. Units of avr. and std. are nm s^{-1} .

Shot		avr.	std.	smb (cal.)	smb (obs.)
M10	noise	7.4	7.1	—	—
	direct <i>P</i>	375.6	101.1	0.93	0.56
	<i>P</i> coda	140.2	73.6	0.78	0.13
M10R	noise	5.1	3.1	—	—
	direct <i>P</i>	414.8	127.0	0.91	0.55
	<i>P</i> coda	107.6	55.6	0.79	0.067

case of both amplitude and waveform shape being identical to those of any station in the array. However, the standard deviations of the amplitudes listed in Table 1 are more than 50 per cent of the average value. This deviation is a factor of decreasing semblance value. If the waveforms have identical shapes but different amplitudes, the expected semblances are

the values noted in Table 1. The semblance values are higher than the values actually obtained in our analysis. Therefore, the causes of the semblance value dropping are the low correlation of waveforms among stations and insufficient static correction. The ratio of the theoretical value to the obtained value for the *P* coda wave is much higher than that for the direct *P* wave. This might be caused by scattered waves from many directions as a result of crustal inhomogeneity.

6 DISCUSSION

Nishimura *et al.* (2000) showed that a temporal change of shallow crustal structure accompanied the *M*6.1 earthquake by analysing waveform data at several seismic stations located just to the north of the epicentre for M10 and M10R. They estimated that a velocity decrease of 0.3–1 per cent appeared just above the earthquake fault. They explained the change by a decrease in confining pressure due to stress drop because of the earthquake. In the present analysis, such a small velocity decrease cannot be detected because of the difference in the ray paths that we used in the analysis. Most of the ray paths approaching the array are different from those in the study of Nishimura *et al.* (2000). Furthermore, data from a single station cannot detect the location change of scatterers such as that obtained in this study, because the coda part of a seismogram cannot be decomposed into scattered waves coming from directions from single-station data alone.

As previously, described, both seismic and volcanic activity were very high in this area for the period of the array observation. According to strainmeter and GPS tiltmeter observations, the pressure origin needed to explain the observed crustal deformation data is estimated at several kilometres depth to the west of Mt Iwate until August 1998. Seismic activity around the Iwate volcano became high from January 1998. According to Tanaka *et al.* (1999), numerous shallow earthquakes occurred in June and July 1998 in the western part of the volcano (to the north of the *M*6.1 earthquake). Moreover, the activity of the low-frequency microearthquakes at about Moho depth had become high since July; however, after August, the shallow earthquake activity lessened, and then the *M*6.1 earthquake occurred on September 3. Seismic activity around the Iwate volcano shifted eastwards by several kilometres during the time between the M10 and M10R events. The estimated scatterer location also changed towards the east. The amount of location shift for the seismic activity is similar to that for the scatterer. This suggests that there exists some relationship between the shift of a seismically active area and changes in inhomogeneous structure, although we cannot show a clear relationship between the two factors.

7 CONCLUSIONS

Waveform analysis for two explosions before and after the *M*6.1 earthquake shows a temporal variation of crustal inhomogeneity based on the dense seismic array observation data. Slant-stacked waveforms are different for the two explosions, and this difference shows that the scatterer location shifted towards east and to greater depths over only three months. We infer that the shift of the scatterer location over such a short passage of time is attributable to the behaviour of fluid in the crust. This temporal change could be related to the change in seismic and/or volcanic activity during the array observation.

ACKNOWLEDGMENTS

We are indebted to the Research Group for Intra-Plate Earthquakes and the Research Group for Explosion Seismology for their efforts in carrying out explosion experiments. We would like to express our appreciation to two reviewers for many helpful suggestions. We also wish to thank Dr. Umino of Tohoku University, who provided us with facilities to collect the hypocentre data. The array observation was carried out by scientists of Akita University, National Research Institute for Earth Science and Disaster Prevention, Tohoku University, and Utsunomiya University. We wish to acknowledge all the participants in the observations for their cooperation. This study was partially supported by Grant-in-Aid for Scientific Research (C), the Ministry of Education, Science, Sports and Culture, Japan (project no. 11650958).

REFERENCES

- Got, J.L. & Fréchet, J., 1993. Origins of amplitude variations in seismic doublets: source or attenuation process?, *Geophys. J. Int.*, **114**, 325–340.
- Hasegawa, A. & Hirata, N., 1999. Northeastern Japan transect—deformation process of the crust and crustal activity in the island arc, *Chikyu*, **27**, 5–11 (in Japanese).
- Hasegawa, A. & Yamamoto, A., 1994. Deep, low-frequency micro-earthquakes in or around seismic low-velocity zones beneath active volcanoes in northeastern Japan, *Tectonophysics*, **233**, 233–252.
- Hirata, N., *et al.*, 1998. The 1998 seismic profiling in the Ou-u Backbone Range, Japan, *Prog. Abstr. seism. Soc. Japan 1998 Fall Mtg*, **A42** (in Japanese).
- Karageorgi, E., McEvilly, T.V. & Clymer, R., 1997. Seismological studies at Parkfield IV: variations in controlled-source waveform parameters and their correlation with seismicity, 1987 to 1995, *Bull. seism. Soc. Am.*, **87**, 39–49.
- Matsumoto, S., Obara, K. & Hasegawa, A., 1998. Imaging P-wave scatterer distribution in the focal area of the 1995 M7.2 Hyogo-ken Nanbu (Kobe) Earthquake, *Geophys. Res. Lett.*, **25**, 1439–1442.
- Matsumoto, S., Obara, K., Yoshimoto, K., Saito, T., Hasegawa, A. & Ito, A., 1999. Imaging of inhomogeneous structure of the crust beneath Ou Backbone Range, northeastern Japan, based on small aperture seismic array observation, *Zisin*, **2**, 283–297 (in Japanese with English abstract).
- Miura, S., Ueki, S., Sato, T., Tachibana, K. & Hamaguchi, H., 2000. Crustal deformation associated with the 1998 seismo-volcanic crisis of Iwate Volcano, north eastern Japan, as observed by a dense GPS network, *Earth Planets Space*, in press.
- Nakamura, A., Hasegawa, A., Hirata, H., Iwasaki, T. & Hamaguchi, H., 2000. An attempt to detect temporal variations of seismic velocity before and after 1998 M6.1 Shizukuishi earthquake, *PAGEOPH*, submitted.
- Nishigami, K., 1991. A new inversion method of coda waveforms to determine spatial distribution of coda scatterers in the crust and uppermost mantle, *Geophys. Res. Lett.*, **18**, 2225–2228.
- Nishigami, K., 2000. Deep crustal heterogeneity along and around the San Andreas fault system in central California and its relation to the segmentation, *J. geophys. Res.*, **105**, 7983–7998.
- Nishimura, T., Uchida, N., Sato, H., Ohtake, M., Tanaka, S. & Hamaguchi, H., 2000. Temporal changes of the crustal structure associated with the M6.1 earthquake on September 3, 1998, and the volcanic activity of Mount Iwate, Japan, *Geophys. Res. Lett.*, **27**, 269–272.
- Poupinet, G., Ellsworth, W.L. & Fréchet, J., 1984. Monitoring velocity variation in the crust using earthquake doublet: an application to the Calaveras fault, California, *Geophys. J. R. astr. Soc.*, **89**, 5719–5731.

- Revenaugh, J., 1995. A scattered-wave image of subduction beneath the transverse range, *Science*, **268**, 1888–1892.
- Research Group for Explosion Seismology, 1999. Seismic refraction/wide-angle reflection experiment in the backbone range of northern Honshu, Japan, *Abstr. Japan Earth planet. Sci. Joint Mtng*, sk-013 (in Japanese).
- Sato, H., 1988. Temporal change in scattering and attenuation associated with the earthquake occurrence—a review of recent studies on coda waves, *PAGEOPH*, **126**, 465–497.
- Sato, M. & Hamaguchi, H., 1999. Analyses of crustal deformation of Mount Iwate observed for a period from February to August 1998, *Chikyu*, **21**, 312–317 (in Japanese).
- Tanaka, S., Nakamichi, H., Hamaguchi, H. & Ueki, S., 1999. The 1998 seismic activity of Mount Iwate, *Chikyu*, **21**, 273–279 (in Japanese).
- Ueki, S., Miura, S., Sato, T., Tachibana, K. & Hamaguchi, H., 1999. The 1998 activity of crustal deformation of Mount Iwate detected by a dense GPS network observation, *Chikyu*, **21**, 296–302 (in Japanese).
- Umino, N., *et al.*, 1998. Aftershock distribution for the M6.1 earthquake of 3 September 1998 in Shizukuishi, Iwate prefecture, north-eastern Japan, *Active Fault Res.*, **17**, 1–8 (in Japanese with English abstract).